CRYSTAL GROWTH & DESIGN

ACS AuthorChoice

Article

pubs.acs.org/crystal

The Epitaxial Growth of Self-Assembled Ternaphthalene Fibers on Muscovite Mica

Clemens Simbrunner,*[,†] Günther Schwabegger,[†] Roland Resel,[‡] Theo Dingemans,[¶] and Helmut Sitter[†]

[†]Institute of Semiconductor and Solid State Physics, Johannes Kepler University, Altenbergerstrasse 69, A-4040 Linz, Austria

[‡]Institute of Solid State Physics, Graz University of Technology, Petersgasse 16, A-8010 Graz, Austria

[¶]Faculty of Aerospace Engineering, Delft University of Technology, 2629 HS Delft, The Netherlands

Supporting Information

ABSTRACT: The morphology and structure of 2,2′:6′,2″-ternaphthalene (NNN) deposited on muscovite mica(001) substrates was investigated by scanning force microscopy (SFM) and specular X-ray diffraction measurements. Consistently, both methods reveal the coexistence of needle-like structures with a {111} contact plane and {001} orientated island-like crystallites, which are built up by almost upright standing NNN molecules. Both orientations are characterized by a well-defined azimuthal alignment relative to the substrate surface, which is analyzed by X-ray diffraction pole figure (XRD-PF) measurements. Based on XRD-PF and SFM analysis, the azimuthal alignment of {001} orientated crystallites is explained by ledge-directed epitaxy along the fibers' sidewalls. These fibers are found to orient along two dominant directions, which is verified and explained by a doubling of the energetically preferred molecular adsorption site by mirror symmetry of the substrate surface. The experimental findings are confirmed by force-field simulations and are discussed based on a recently reported growth model.

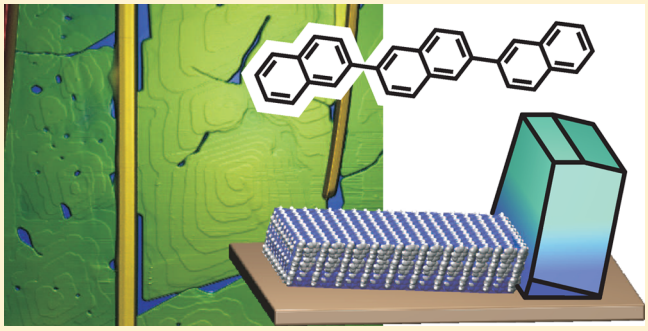

INTRODUCTION

When deposited on various substrate surfaces, rod-like, π-conjugated, small organic molecules are well-known for their tendency to form highly anisotropic crystal shapes, which are frequently called fibers or needles.[1−18] Whereas the epitaxial growth has been studied on various substrates, in particular anisotropic surfaces seem favorable to conserve the highly anistropic morphology and optical properties, for example, polarized emission or adsorption provided by a parallel molecular orientation obtained by self-assembly.[19,20] Consequently, Cu(110),[21−23] TiO_2(110)[24] and muscovite mica(001)[4,25−27] are frequently chosen as a proper fundament to study the epitaxial growth of rod-like small molecules.

In this paper, the epitaxial growth of 2,2′:6′,2″-ternaphthalene (NNN) on muscovite mica(001) is reported. As indicated in Figure 1a, the molecule is built from three naphthalene units, which are linked together by C−C bonds. Based on morphological and structural analysis, the coexistence of needle-like structures and island-like crystallites is verified. Structural analysis reveals two different crystal orientations. Whereas island-like structures are built up by upright standing molecules orientated with a (001) contact plane relative to the muscovite mica substrate (see Figure 1b), needles consist of NNN molecules with a (111) lying orientation (see Figure 1c). Both crystal configurations provide a well-defined azimuthal alignment, which is discussed based on force field simulations and a recently reported growth model.[26] The azimuthal alignment of island like structures is explained by "ledge directed" epitaxy at the fiber sidewalls.

EXPERIMENTAL SECTION

Chemical Synthesis of 2,2′:6′,2″-Ternaphthalene (NNN). 2,2′:6′,2″-Ternaphthalene (NNN) was prepared using standard Suzuki cross-coupling procedures.[28−30] This all-aromatic compound could be obtained in high yield by coupling 2 equiv of 2-naphthaleneboronic acid (1) with 1 equiv of 2,6-dibromonaphthalene (2), as described in the Supporting Information. The final product, 2,2′:6′,2″-ternaphthalene (NNN), was obtained as a colorless product, which appears to be highly insoluble in common solvents and could only be recrystallized from 1,2,4-trichlorobenzene (colorless platelets). The material was checked with gas chromatography and mass spectroscopy and found to be >99% pure before thermal sublimation. The yield was 91% after recrystallization from 1,2,4-trichlorobenzene.

Sample Preparation. All samples have been fabricated on muscovite mica(001) substrates (SPI, Structure Probe, Inc.). Muscovite mica is a representative of sheet silicate minerals and provides a layered structure of aluminum silicate sheets weakly bound by layers of potassium ions. Each layer is characterized by a high symmetry direction identified by parallel aligned surface grooves. Between the individual sheets, the high symmetry direction alternates by 120° leading to a periodic $\alpha\beta\alpha\beta$ stacking sequence along [001]

Received: June 17, 2013
Revised: November 7, 2013
Published: January 7, 2014

   dx.doi.org/10.1021/cg400912t | *Cryst. Growth Des.* 2014, 14, 442−449

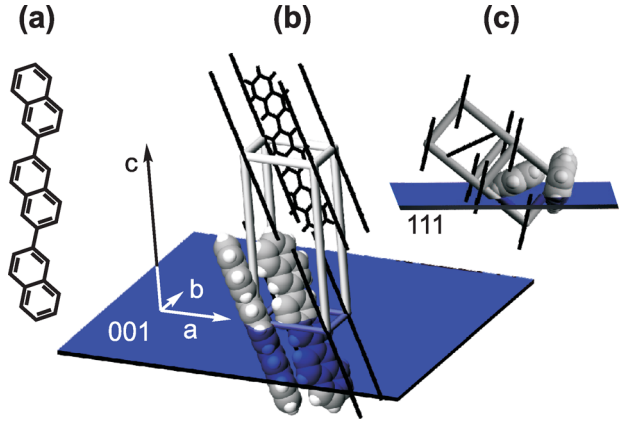

Figure 1. (a) The molecular structure of 2,2′:6′,2″-ternaphthalene (NNN). (b) A side view of NNN molecules packed in the observed crystal structure. Each unit cell houses two NNN molecules. Molecules are approximately standing on the S (001) contact plane, which is indicated in blue. (c) A side view along the long molecular axis visualizing the edge-on/flat-on herringbone stacking of NNN. The blue area represents the orientation of the B (111) contact plane where molecules are aligned in almost in lying configuration.

direction.[25] Immediately after cleaving, the mica substrates were transferred to the hot wall epitaxy (HWE) chamber.

The HWE technique was applied for the deposition of the organic material, which allows us to perform the growth process close to thermodynamic equilibrium, and in further consequence relatively high vapor pressure of the organic deposit in the substrate region can be achieved. Therefore, the requirements concerning vacuum conditions are reduced compared with, for example, molecular beam epitaxy.[31] The source material NNN was purified twice by thermal sublimation before filling it into the quartz tube of the HWE reactor. Muscovite mica substrates were transferred into the deposition chamber via a load lock and subsequently preheated at the deposition temperature (80 °C) for 30 min to ensure a stable temperature during the whole deposition process. The deposition was performed thereafter under a base pressure of 9×10^{-6} mbar.

Morphological Investigation. Optical microscope images have been acquired by a Nikon Labophot 2A microscope in combination with a Nikon type 115 digital camera. Scanning force microscopy (SFM) studies of the deposited organic films were performed using a Digital Instruments Dimension 3100 in the tapping mode. The 10×10 μm^2 images have been acquired at scan speeds of 4−6 μm/s using SiC tips (μmasch, HQ:NSC15/Al BS) exhibiting a cone angle of 40°. Nominal values for resonance frequency and tip radius are 325 kHz and 10 nm, respectively.

X-ray Diffraction Experiments. X-ray diffraction (XRD) measurements were carried out on a Philips X'pert X-ray diffractometer using Cr Kα radiation (λ = 2.29 Å) and a secondary graphite monochromator. Please note that the monochromator is transparent for λ, $\lambda/2$, $\lambda/3$, etc., so despite the weak intensity of the Bremsspektrum, it can give clear Bragg peaks due to the scatting on the single crystalline mica substrate. Specular scans were performed in Bragg−Brentano configuration by varying the z-component of the scattering vector **q**. Consequently it is possible to detect lattice planes that are parallel to the sample surface. X-ray diffraction pole figure measurements were performed in Schultz reflective geometry.[32] Pole figures were acquired by measuring at a constant length of **q** and only

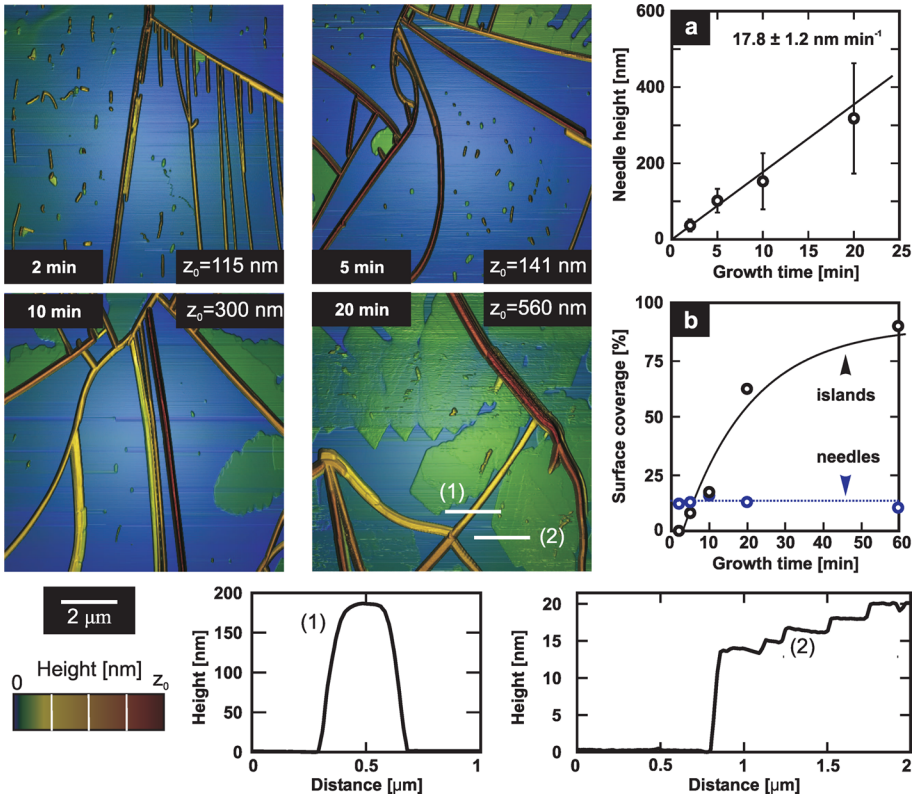

Figure 2. Scanning force microscopy (SFM) images showing the sample morphology versus deposition time. All samples are dominated by needle-like structures. With increasing growth time, island-like structures start to nucleate at the needle side walls covering continuously the substrate surface between the fibers. Exemplary cross sections for both morphologies are indicated in the bottom part of the figure. As indicated in part a, the height of the fiber like structures linearly increases with growth time reaching values of some 100 nm. Contrarily, the surface coverage by needles stays approximately constant (part b). Island-like structures are characterized by steplike morphology. Step heights in the center part of the islands approximately correspond to a monolayer of upright standing molecules.

dx.doi.org/10.1021/cg400912t | *Cryst. Growth Des.* 2014, 14, 442−449

varying its direction. The unit cell parameters of NNN, which were used for analysis, are defined by a = 8.148 ± 0.005 Å, b = 5.978 ± 0.005 Å, c = 19.45 ± 0.2 Å, and β = 94.6 ± 0.2° describing a monoclinic lattice ($P2_1/a$).[33] The unit houses two NNN molecules in planar configuration.

Force Field Simulations. The van der Waals (vdW) interaction between the organic molecule and the dielectric substrate is modeled by Lennard-Jones-type potentials. Corresponding parameters are taken from the Universal Force Field[34] implemented in a Matlab program. The molecules and substrates are assumed to be rigid where the internal structure of an isolated NNN molecules is determined from the crystal structure.[33] Simulations were performed for the adsorption of a single NNN molecule as well as a crystal stack. By assuming that a single NNN molecule prefers to lie flat on the surface, the energy minimization procedure is simplified in the following way: We consider only four molecular degrees of freedom, the x-, y-, and z-positions of the molecular center of mass and the angle φ. The angle φ defines the azimuthal molecular alignment and is probed by rotating the NNN molecule around the z-axis (surface normal). We perform a grid-based optimization to search for the best molecular adsorption geometry using a grid of 81 × 81 points for the lateral position. The adsorption distance was varied between 2.9 and 3.1 Å. The adsorption angle was tested with a step size of $\Delta\varphi$ = 1°. The surface structure of the substrate has been assumed to be the same as in the bulk where the corrugation is about 0.2 Å. The substrate surface is assumed to be terminated by the tetrahedral layer of muscovite mica. For the simulation of the 7 × 2 NNN stack, the molecular packing has been deduced from the crystal structure[33] of a (111) orientated NNN crystallite. Due to the presence of flat and edge-on molecules, the adsorption distance has been optimized, yielding a distance of 1.6 Å of the lowest H atom of edge-on NNN molecules to the substrate surface. Because energetic minima are significantly narrow for the molecular stack, an angular resolution of $\Delta\varphi$ = 0.5° has been chosen for the calculations.

EXPERIMENTAL RESULTS

Epitaxial Growth on Muscovite Mica(001). In a first step, NNN was deposited by hot wall epitaxy (HWE) on muscovite mica(001). Whereas the substrate temperature was kept constant at 80 °C, the deposition time was continuously increased. Scanning force microscopy was chosen to study the sample morphology versus deposition time, and obtained images (10 × 10 μm^2) are depicted in Figure 2. As the maximum height scale z_0 significantly changes with increasing deposition time, the corresponding values are indicated for each sample. The morphology of all samples is dominated by the presence of several micrometer long needle like structures that are aligned along multiple orientations. As exemplified by the cross-section (1), these fibers reach height levels up to ∼200 nm and are characterized by similar dimensions in width. A more detailed analysis is provided in Figure 2a, plotting the mean needle height versus growth time. As indicated by the solid line, the growth rate can be approximated by a linear fit, yielding a slope of ∼17.8 ± 1.2 nm·min^{-1}. Interestingly, the fibers' surface coverage is approximately constant for the whole sample series yielding a value of ∼12.5%.

The SFM analysis reveals that flat islands start to nucleate at the side walls of the fibers and continuously fill the substrate surface between the fibers with increasing deposition time. The latter observation is underlined by analyzing the islands' surface coverage, which is depicted in Figure 2b as a function of growth time. The solid line, which represents a guide for the eye, indicates an asymptotic approach to ∼85% of the surface area. Again, a representative sample position has been chosen to deduce a cross-section (2), which is presented in the bottom right of Figure 2. As reported for other rod-like molecules,[4,35−39] a steplike morphology with height levels in the range of 1.8−2 nm are observed in the inner parts of the islands. The obtained value corresponds to approximately one monolayer of upright standing NNN molecules. Contrarily, the step size of the boundary, defined by the islands and the substrate surface, is significantly larger reaching values in the range of ∼15 nm. These steps are further characterized by straight extensions, which suggest the formation of well-defined crystal facets.

In a next step, X-ray diffraction (XRD) has been chosen to study the structural properties of the organic crystallites. In order to obtain sufficient diffraction intensity, a sample with 216 nm high NNN fibers has been selected. Figure 3a reports the acquired specular XRD diffraction pattern, which is

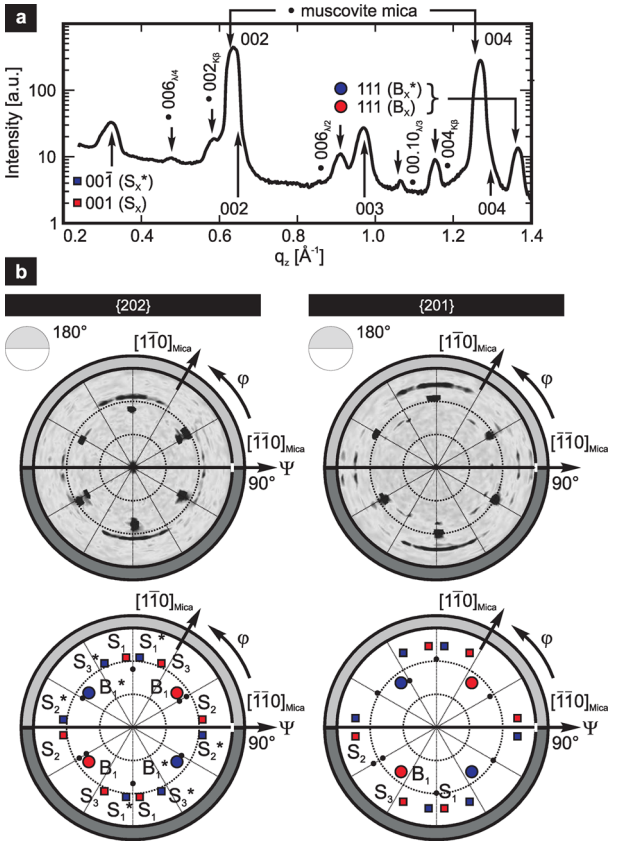

Figure 3. (a) Specular X-ray diffraction (XRD) spectrum of NNN on muscovite mica(001). Scanning force microscopy images revealed a needle height of 216 nm for the chosen sample. The spectrum is dominated by a series of S (001) diffractions peaks, which are representative for island-like morphologies. Additionally, contributions of B (111) orientations are indicated. Peaks originating from the muscovite mica substrate are indicated by black solid circles. (b) XRD pole figure (XRD-PF) analysis of {202} and {201} diffraction peaks, providing information about the azimuthal crystal orientation. As indicated by the simulated pole distribution (bottom), all diffraction spots can be explained by the presence of three differently aligned (001) crystallites, labeled as S_{1-3} (red). The mirror symmetry plane of the muscovite mica (001) surface is indicated by a horizontal line, which explains the presence of mirrored S^*_{1-3} crystallites (blue) with a (00$\bar{1}$) contact plane. Moreover, XRD-PF reveal a well-defined azimuthal orientation of B_1 (111) crystallites (red circles). Again mirror symmetric crystallites B_1^* ($\bar{1}\bar{1}\bar{1}$) are indicated by blue symbols. Diffraction intensities from the muscovite mica substrate are indicated by black solid filled circles.

dx.doi.org/10.1021/cg400912t | Cryst. Growth Des. 2014, 14, 442−449

dominated by a series of {00n} diffraction peaks. These peaks are characteristic for island-shaped crystal morphologies, built up by approximately standing NNN molecules, and are consequently abbreviated by S-orientations (q_{001} = 0.324 Å^{-1}). Arrows in the upper part of Figure 3a indicate the positions of (00.2n) diffraction peaks stemming from the muscovite mica(001) substrate. Additionally, a diffraction peak arises at q_z = 1.36 Å^{-1} ,which correlates with (111) orientated NNN crystallites, abbreviated as B orientation. The orientation is characteristic for a nearly flat lying molecular configuration and thus explains the presence of needle-like crystallites as revealed by SFM analysis. A more detailed analysis is reported in the Supporting Information.

In order to analyze the azimuthal alignment of the NNN crystallites relative to the muscovite mica(001) substrate, XRD-PF measurements have been performed and are reported in Figure 3b. For a profound analysis, XRD-PF have been acquired with a maximum sensitivity to diffraction intensities stemming from the scattering at {202} and {201} netplanes and are depicted in the bottom leftand right part of Figure 3b.

The diffraction intensities show a distinct azimuthal distribution, which underlines a well-defined epitaxial relationship to the muscovite mica substrate. The obtained symmetry of the diffraction intensities further underlines the presence of an α terminated muscovite mica surface, which is characterized by a mirror plane along the $[\bar{1}10]_{mica}$ orientation. The orientation of the substrate has been determined from diffraction patterns stemming from muscovite mica (001) and are indicated by black solid circles. XRD-PF patterns of the organic crystallites can be constructed by mirror operation from the top hemisphere, sketched by a gray shaded sector. Moreover, the XRD-PF patterns reveal a 2-fold rotational symmetry, which can be understood by an approximately equivalent adsorption energy for 180° turned organic crystallites. Consequently, discrimination between both crystal alignments has been omitted and simulated 2-fold symmetric diffraction spots are labeled identically. Based on these geometrical considerations, only the diffraction spots of a single quadrant have to be analyzed and labeled.

Diffraction intensities that are characteristic for S-orientated crystallites are located at Ψ = 63° (74°) in the left (right) XRD-PF, and their azimuthal distribution can be explained by the presence of three crystal orientations labeled as S_{1-3}. Consistently, both XRD-PF measurements hint the strongest diffraction intensities originating from S_1 crystallites. Diffraction spots, which can be attributed to B* ($\bar{1}\bar{1}\bar{1}$)/B (111) crystallites are expected to appear at Ψ ≈ 51° for both diffraction geometries and are marked by blue/red filled circles. As each quadrant reveals the presence of one diffraction spot, the azimuthal alignment of B orientated fibers can be constructed from a single crystallite B_1. Again, mirror symmetric crystals are labeled as B_1^* and are characterized by a ($\bar{1}\bar{1}\bar{1}$) contact plane.

Based on the simulated XRD-PF diffraction peaks, the long needle axis (LNA) and long molecular axis (LMA) orientations of B orientated fibers have been deduced and are presented in Figure 4 by solid filled arrows. Whereas the LNA coincides with the $[1\bar{1}0]$ orientation, the LMA can be approximated by the alignment of $[10\bar{1}]$ relative to the muscovite mica substrate. Mirror symmetry of the muscovite mica substrate leads to the generation of two energetically equivalent crystallites.[26] Fibers that are built up by B_1^* (111) orientated crystallites (blue) are aligned with their LNA (LMA) −59.5° (49°) relative to the muscovite mica substrate's $[\bar{1}10]_{mica}$ crystallographic orientation. Contrarily, their mirror symmetric twins (B_1) can be constructed by flipping the B_1^* crystallites upside down (red arrows), azimuthally aligned with their LNA (LMA) 59.5° (−49°) relative to $[\bar{1}10]_{mica}$. In order to verify the LNA alignment, which has been constructed based on XRD-PF measurements, optical microscopy has been chosen, and an image of a representative sample area is depicted in Figure 4. The sample morphology is dominated by fibers that are aligned in a V-shaped, herringbone fashion. As indicated by large red and blue arrows, which represent the expected B_1 and B_1^* LNA orientations deduced by XRD-PF analysis, sample morphology perfectly matches with the structural data analysis. Nevertheless, additional needle orientations, which are present in minor fraction, can be observed and are marked by small red (B_2) and blue (B_1^*) arrows, respectively. In order to gain better statistics, a microscopy image of a larger sample area has been chosen to perform a fast Fourier transformation (FFT) and the obtained pattern is depicted beside. The FFT is dominated by two stripes, which are characterized by an enclosing angle that perfectly reflects the LNA orientation of B_1 and B^*_1 crystallites (indicated by red and blue arrows).

In a next step, the epitaxial relationship of S_{1-3} crystallites has been analyzed. In particular, the azimuthal alignment of their $[1\bar{1}0]$ directions has been deduced and is depicted in the outer ring of Figure 4 (LNA). Because S_1 and S_1^* crystallites represent the major fraction, they are indicated by large arrows

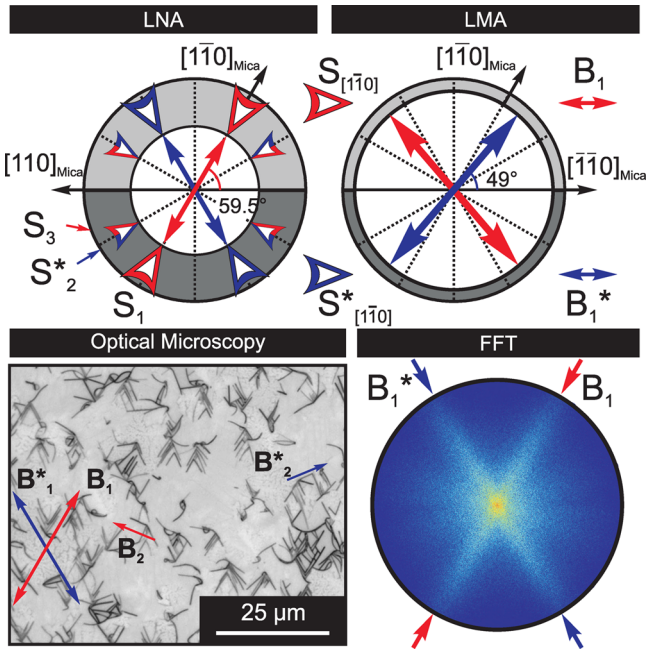

Figure 4. Long needle axis (LNA) (left) and long molecular axis (LMA) (right) orientations of B_1 (red solid filled arrows) and mirror symmetric B_1^* (blue solid filled arrows) crystallites, deduced by X-ray pole figure (XRD-PF) measurements. In the outer ring of the LNA polar plot, additionally the $[1\bar{1}0]$ crystallographic orientations of S_{1-3} (red) and S_{1-3}^* (blue) crystallites are indicated. It is visualized that the $[1\bar{1}0]$ crystallographic direction of S_1 crystallites provides the same azimuthal orientation as the LNA of B_1 fibers. Below, the obtained LNA orientations are verified by the observed sample morphology using optical microscopy. Beside B_1 and B_1^* fibers additionally minor fractions of approximately horizontally aligned crystallites are observed (marked by small red and blue arrows). By using fast Fourier transformation (FFT) (depicted beside), the dominant fraction of B_1 and B_1^* crystal orientations is further underlined.

dx.doi.org/10.1021/cg400912t | Cryst. Growth Des. 2014, 14, 442−449

approximately aligned ±60° relative to $[\bar{1}10]_{mica}$. The azimuthal orientation perfectly coincides with the LNA of B_1 and B_1^* crystallites, which already suggests an epitaxial relationship of both crystal types. In order to analyze the latter observation in more detail, a representative SFM has been chosen and is discussed in the following paragraphs.

The SFM image, which is shown in Figure 5, is dominated by two approximately vertically aligned fibers. Between fibers, the

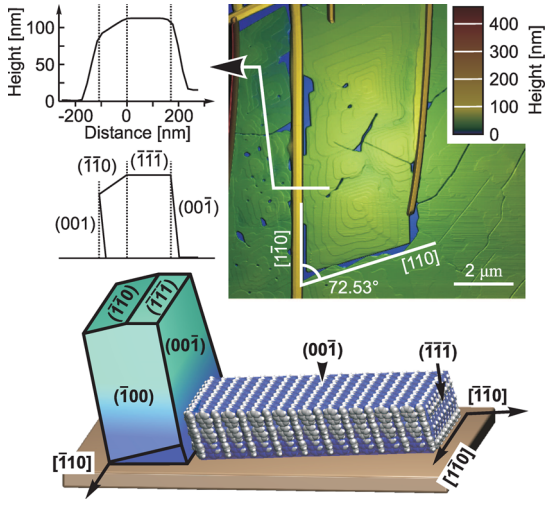

Figure 5. Scanning force microscopy (SFM) image showing vertically aligned fibers and S orientated islands in between after the deposition of 60 min NNN at 80 °C substrate temperature. The island's boundaries correlate with the geometrical alignment of [110] and $[1\bar{1}0]$ orientations. The extracted fiber cross-section (top, left) can be explained by the formation of $(\bar{1}\bar{1}\bar{1})$, $(\bar{1}\bar{1}0)$ and ±(001) facets. Based on the observed crystal shapes, their crystallographic orientations relative to each other has been deduced and is visualized by a 3D model below. The epitaxial relationship between fibers and islands is consistent with the structural analysis and can be explained by a nucleation of NNN molecules at the fiber side walls, also called "ledge directed epitaxy".

presence of an S orientated island can be observed, which is terminated in the bottom part of the image by a sharp L-shaped boundary. The observed boundary shape perfectly correlates with the expected angle between the [110] and $[1\bar{1}0]$ crystallographic orientations of an $(00\bar{1})$ orientated crystallite. The generation of the observed crystal shape can be understood by the formation of $\pm(1\bar{1}n)$ and $\pm(11n)$ side facets, which represent low index planes for $n = \bar{1}$, 0, or 1.

An extracted cross-section of the observed fiber is presented in the left part of Figure 5. The observed fiber is terminated in the right part by a flat plane, which is aligned parallel to the substrate at a height of approximately 100 nm. Contrarily, the left side of the fiber shows a constantly decreasing height level. The slope of the side facet approximately correlates with a 25 nm decrease in height along 100 nm of the needle width (~14°). The LNA of B* type crystallites is defined by their $[1\bar{1}0]$ orientation and consequently all crystallographic planes $\pm(11n)$ are aligned parallel to it. Because the angular tilt of 13.8° between the low index planes $(\bar{1}\bar{1}0)$ and $(\bar{1}\bar{1}\bar{1})$ perfectly correlates with the observed SFM analysis, the theoretically expected cross-section of a B_1^* fiber has been modeled and is depicted below the experimental data. Although, the observed steep height decrease at the fiber side walls is below the resolution limit of the SFM, a termination of the fibers by (001) and $(00\bar{1})$ facets can be assumed.[40]

Based on the latter analysis, a three-dimensional model of both crystal types has been generated and is depicted in the bottom part of Figure 5. As indicated by the XRD-PF analysis, which is presented in Figure 4 (LNA), B_1^* and S_1^* crystallites shared the same azimuth for their crystallographic $\pm[1\bar{1}0]$ orientations. In that way, the tilt angle of standing NNN molecules within the S-type crystallite approximately correlates with the tilt angle of the fiber (001) low energy plane. Analogous observations were demonstrated for 6T fibers and are explained by the nucleation of islands at the sidewalls of already existing needles.[4,37] Moreover, the latter picture is perfectly consistent with the SFM analysis presented in Figure 2, which reports a continuously increasing island coverage for longer deposition times. Such epitaxial alignment based on a geometrical fit between nucleating crystallites and already existing topographic features on the substrate is called "ledge directed epitaxy".[41,42] Based on the latter analysis together with XRD-PF data presented in Figure 4 (LNA), it can be concluded that the minor fraction of S_{2-3} crystallites has most likely nucleated at B-type fibers, which are orientated approximately ±30° tilted relative to $[\bar{1}10]_{mica}$ of the muscovite mica substrate. This conclusion is further consistent with the microscopy image, presented in Figure 4, revealing the presence of a minor fraction of such fibers (below the detection limit of XRD-PF measurements), which are subsequently labeled by B_2 and B_2^*.

DISCUSSION

In order to understand the observed growth behavior of B_1 and B_2 fibers on muscovite mica(001), the left part of Figure 6 depicts a planar NNN molecule in gas phase. Analogous to 6T,[43] a planar molecule is characterized by a mirror plane σ_h, which is aligned in the plane of the naphthalene rings, and a 2-fold rotational axis, which is aligned normal to σ_h. Consequently, the atomic arrangement follows C_{2h} point group symmetry. For further consideration, it should be assumed that single NNN molecules tend to adsorb lying flat on the muscovite mica substrate in order to maximize their contact area. In that way, σ_h is orientated parallel to the substrate, and the molecule becomes chiral when adsorbed on an arbitrary surface. Molecules that are intrinsically achiral but obtain a form of 2D chirality when adsorbed on a substrate surface are also called prochiral.[44] Analogous to 6T,[26,45] two mirror symmetric NNN enantiomers (sketched as red and blue molecules) can adsorb on the muscovite mica surface, which cannot be brought into congruence by translation and rotation.

Taking a top view of the molecular stacking at the contact plane of B-type crystallites, which is depicted in the right panel of Figure 6, reveals that (111) orientated fibers are built up by an alternating assembly of only one enantiomer (red) and edge-on NNN molecules. Contrarily, their twin crystallites B* $(\bar{1}\bar{1}\bar{1})$ are built up by the mirrored molecular configuration (blue) only. The latter observation further explains the consistent choice of a red and blue color code for molecules and crystallites. Beside a real space model for B_1 crystallites, which is deduced by XRD-PF analysis, the right part of Figure 6 further includes the proposed geometry of B_2 fibers. Based on a growth model that has been deduced for 6T fibers,[26] it is assumed that two needle orientations, for example, B_1 and B_2^* can originate from one molecular adsorption site. The existence of these two LNA orientations is explained by a mirror symmetric molecular

dx.doi.org/10.1021/cg400912t | Cryst. Growth Des. 2014, 14, 442−449

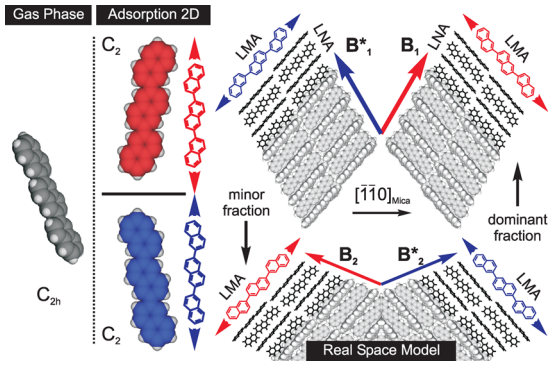

Figure 6. Molecular symmetry of a planar NNN in gas phase and when adsorbed flat on an arbitrary surface. Due to the presence of a mirror symmetry plane σ_h parallel to the naphthalene rings and a 2-fold rotational axis, aligned normal to it, the NNN molecule in gas phase can be described by the C_{2h} point group. Contrarily, when adsorbed flat on a substrate surface, NNN can form two mirror symmetric enantiomers (sketched by red and blue molecules), which follow C_2 symmetry. The right panel depicts a real space model of the discussed crystal orientations (top view). The molecular alignment of NNN within the surface unit cell has been deduced from its bulk structure, oriented with a (111)/($\overline{1}\overline{1}\overline{1}$) contact plane for B/B* crystallites. The orientation of the long molecular axis (LMA) or long needle axis (LNA) is indicated by blue or red arrows. Taking a closer look at the molecular stacking at the contact plane of B-type crystallites reveals that (111) orientated crystals are alternately assembled by red enantiomers and edge-on NNN molecules. Contrarily, their mirror symmetric twins B* only consist of blue molecular configurations. The real space image of B_1 (B_1^*) and B_2^* (B_2) crystallites further underlines a parallel molecular alignment but opposite stacking direction.

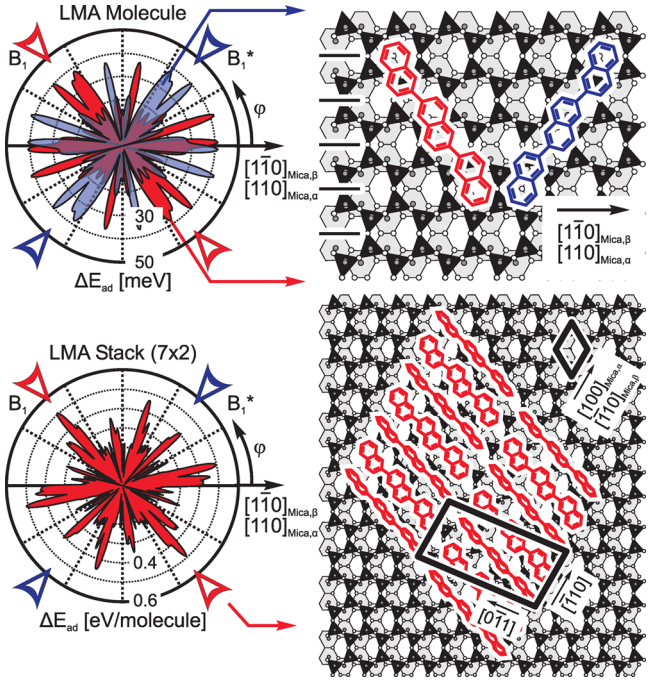

Figure 7. The adsorption energy as a function of the long molecular axis (LMA) orientation (φ) is depicted in the top panel in terms of a polar plot. Red- and blue-filled curves show the result for both NNN enantiomers. Red and blue arrows indicate the molecular orientation deduced by experiments. At the indicated positions, force field simulations reveal a broad maximum for the corresponding enantiomer. Contrarily, the adsorption site seems less favorable for the mirror symmetric molecule ($\Delta E \approx 20$ meV). A real space model that sketches the lateral position for the molecular adsorption angle at $\varphi = \pm 57°$ is depicted beside. Simulations reveal a preferred alignment of the terminating naphthalene units in the surface corrugations of the muscovite mica substrate (indicated by horizontal lines). Below, an analogous analysis has been done for a 7 × 2 molecular stack representative for the contact plane of a B (111) crystallite. Simulations reveal a strongly pronounced adsorption maximum at the experimentally observed adsorption angle (red arrow) and a significantly different adsorption energy for a B* crystal with opposite stacking sequence (blue arrow, $\Delta E \approx 300$ meV/molecule). A real space model of the optimized adsorption position is depicted in the right panel. By comparing the alignment of the NNN molecules with the muscovite mica unit cell, an approximately periodic alignment can be recognized along $[100]_{mica}/[\bar{1}10]_{mica}$ for an α/β terminated surface.

stacking during crystal nucleation. Interestingly, epitaxially grown 6T on muscovite mica showed a comparable fraction of both stacking types, which explains the observation of four LNA orientations. The latter phenomenon is further explained by force field simulations for both crystal types, yielding a similar adsorption energy with a deviation of some milli-electronvolts/molecule.[26] Contrarily, XRD-PF analysis revealed that NNN fibers are dominantly present only in one configuration, which reduces the observed LNA orientations to two (see the FFT in Figure 4). Consequently, it can be stated that both crystal types seem to significantly differ concerning their adsorption energy, which should be investigated and underlined by the discussion of force field simulations within the next paragraphs.

In a first step, the optimal adsorption energy of a single NNN molecule has been deduced based on force-field simulations by selecting the most favorable adsorption site for each angle φ. The angle φ characterizes the azimuthal alignment of the LMA relative to mirror symmetry plane of the muscovite mica substrate surface. The molecules are assumed to adsorb flat on the substrate and the adsorption energy, E_{ad}, is defined as the difference between the energies of the isolated subsystems and the energy of the combined system. Therefore, maxima in the E_{ad} versus φ curves evidence the favorable adsorption geometries. To increase the readability, ΔE_{ad} curves are presented in Figure 7 in terms of a polar plot, where $\Delta E_{ad} = E_0 - E_{ad}$. The parameter E_0 represents the adsorption energy at the least favorable angle φ, yielding a value of $E_0 = -2.49$ eV for the isolated molecules. Because NNN molecules can adsorb either in their left- or right-handed configuration, simulations have been performed for both enantiomers and are color coded by red- and blue-filled curves.

Simulations yield, for both molecular configurations, multiple adsorption maxima, which are located for the blue marked enantiomer at $\varphi_{max,blue} = 42°$, 57°, 102°, 161°, and 178°. Due to 2-fold rotational symmetry of the NNN molecule, identical values are obtained for $\Delta E_{ad}(\varphi+180°)$. Moreover, optimized adsorption positions for the red molecular type are found at $\varphi_{max,red} = -\varphi_{max,blue}$ due to mirror symmetry of the substrate surface. Experimentally obtained adsorption angles are further indicated by a blue (red) arrow at $\varphi = 49°$ (131°). Both adsorption angles correlate with the broadest maxima obtained by simulations and are importantly consistent with the simulations of the corresponding enantiomer. The fact that beside experimentally observed adsorption geometries force field calculations also yield additional maxima is attributed to the usage of empirical potentials, which in some cases may yield the wrong energetic ordering of competing structure

dx.doi.org/10.1021/cg400912t | Cryst. Growth Des. 2014, 14, 442−449

solutions.[46] Nevertheless, it has to be underlined that simulations indicate a significant less favorable adsorption site for the mirror symmetric molecular configuration (~20 meV). In general, adsorption energies for both molecular configurations significantly differ, which in further consequence leads to a nonequal distribution or even breakup of both enantiomers depending on the adsorption angle. Contrarily, simulations as well as experimental data that are reported for 6T[26] indicate a significantly lower energetic splitting between both molecular configurations, which may result from a higher symmetry of the molecule. The latter statement can be understood by the fact that thiophene molecules with an odd ring number, for example, quinquethiophene or septithiophene, are characterized by a mirror symmetry plane when adsorbed on a surface and consequently do not show a prochiral character. Contrarily, the asymmetric alignment of the C−C bond between two naphthalene units of NNN inevitably leads to a prochiral behavior when adsorbed on a substrate surface and consequently plays an essential role concerning the energetic separation of both enantiomers at a defined adsorption angle.

The experimentally confirmed adsorption position of NNN molecules is further depicted in the right part of Figure 7. For both molecules, an adsorption angle $\varphi = \pm 57°$ has been chosen. Analogous to calculations for p-6P and 6T,[26] NNN molecules tend to align their rings in the surface corrugations, which are indicated by vertical solid lines.

In order to study the adsorption energetics of a B-type crystallite, a 7 × 2 molecular stack has been deduced from a (111) orientated crystallite. Analogous to the force field simulations of an isolated molecule, the adsorption energy ΔE_{ad} for the stack has been probed depending on the molecular orientation φ and the adsorption energy at the least favorable adsorption angle is given by $E_0 = -0.41$ eV/molecule. Because the curve calculated for the a B* $(\overline{111})$ stack follows the same behavior as discussed for a single molecule (mirror symmetric), only the results for a B contact plane are depicted in order to increase readability. Interestingly, simulations reveal that not only the number of energetically favorable adsorption sites decreases but also the angular acceptance, which becomes visible by well pronounced peaks. Simulations further indicate the presence of two adsorption maxima, which are located at $\varphi = 12°$ and $-48°$. Again, the experimentally obtained adsorption angle for B_1 crystallites is indicated by a red arrow and underlines a nearly perfect agreement. Moreover, it can be recognized that the adsorption energy for a B_2 crystal (at +48°) becomes even more unfavorable than that for a single molecule, which is manifested by a much lower value of ΔE_{ad} in the range of some 100 meV/molecule.

Consequently, force field simulations not only reflect the experimental observations but also explain the dominant fraction of B_1 crystallites by a preferred nucleation of their stacking sequence in contrast to B_2 crystallites. The observed behavior can be even better understood by analyzing the real space model of the simulated adsorption position at $\varphi = -48°$. Besides the molecular alignment, also the surface unit cells of the muscovite mica and B crystal have been indicated. Obviously, the unit vector $[\overline{1}10]$ of the NNN crystal stack, which also defines its LNA, tends to align parallel to one surface unit vector of the muscovite mica crystal, which is defined by the $[100]_{mica,\alpha}$ ($[\overline{1}10]_{mica,\beta}$) orientation for an α (β) terminated surface.[25]

Summary and Conclusion. The epitaxial growth of ternaphtalene (NNN) on muscovite mica(001) has been investigated by combining structural (XRD-PF) and morphological (SFM) methods. Consistently, both methods reveal the formation of S (001) orientated NNN island-like structures which have nucleated at the sidewalls of B (111) orientated fibers. It is demonstrated that the latter NNN crystal types tend to align along two dominant directions, which leads to the formation of a V-shaped sample fiber morphology. Because the tilt angle of NNN molecules within S-orientated crystallites correlates with the tilt angle of the fiber side facets, the island nucleation is explained by "ledge directed epitaxy". Based on this growth model, it can be understood that both crystal types provide a well-defined azimuthal orientation relative to the muscovite mica substrate.

By use of force field simulations, the growth of the fibers is further analyzed. The epitaxial growth of sexithiophene (6T) on muscovite mica showed the formation of four well-defined fiber orientations, which can be explained by mirror symmetry of the muscovite mica substrate and two differently stacked 6T crystallites, which can nucleate at a molecular adsorption position.[26] Contrarily, experimental investigations indicate that NNN crystallites tend to stack in a single configuration, which explains the dominant formation of only two fiber orientations. Based on force field simulations, the latter observation is further investigated and explained by significantly different adsorption energies of both crystal types. It is further demonstrated that the observed behavior results from an interplay of the molecular adsorption and lattice match.

■ ASSOCIATED CONTENT

Supporting Information

Experimental details concerning the synthesis of 2,2′:6′,2″-ternaphthalene (NNN) and X-ray diffraction analysis. This material is available free of charge via the Internet at http://pubs.acs.org.

■ AUTHOR INFORMATION

Corresponding Author

*E-mail: clemens.simbrunner@jku.at.

Notes

The authors declare no competing financial interest.

■ ACKNOWLEDGMENTS

This work has been financially supported by the Austrian Science Fund (FWF), Grant P25154, and by the federal government of Upper Austria (project "Organische Nanostrukturen").

■ REFERENCES

(1) Balzer, F.; Rubahn, H.-G. *Adv. Funct. Mater.* **2005**, *15*, 17.
(2) Andreev, A.; Matt, G.; Brabec, C.; Sitter, H.; Badt, D.; H, H. S.; Sariciftci, S. *Adv. Mater.* **2000**, *12*, 629.
(3) Balzer, F.; Schiek, M.; Rubahn, H.-G.; Al-Shamery, K.; Lützen, A. *J. Vac. Sci. Technol. B* **2008**, *26*, 1619.
(4) Simbrunner, C.; Hernandez-Sosa, G.; Oehzelt, M.; Djuric, T.; Salzmann, I.; Brinkmann, M.; Schwabegger, G.; Watzinger, I.; Sitter, H.; Resel, R. *Phys. Rev. B* **2011**, *83*, No. 115443.
(5) Yanagi, H.; Morikawa, T. *Appl. Phys. Lett.* **1999**, *75*, 187.
(6) Oehzelt, M.; Grill, L.; Berkebile, S.; Koller, G.; Netzer, F. P.; Ramsey, M. G. *ChemPhysChem* **2007**, *8*, 1707−1712.
(7) Haber, T.; Ivanco, J.; Ramsey, M. G.; Resel, R. *J. Cryst. Growth* **2008**, *310*, 101−109.
(8) Schiek, M.; Balzer, F.; Al-Shamery, K.; Lützen, A.; Rubahn, H.-G. *J. Phys. Chem.* **2009**, *113*, 9601.

(9) Schiek, M.; Balzer, F.; Al-Shamery, K.; Lützen, A.; Rubahn, H.-G. *Soft Matter* **2008**, *4*, 277.
(10) Balzer, F.; Schiek, M.; Lützen, A.; Rubahn, H.-G. *Chem. Mater.* **2009**, *21*, 4759.
(11) Babu, S. S.; Praveen, V. K.; Prasanthkumar, S.; Ajayaghosh, A. *Chem.—Eur. J.* **2008**, *14*, 9577−9584.
(12) Schenning, A. P. H. J.; Meijer, E. W. *Chem. Commun.* **2005**, 3245.
(13) Brownell, L. V.; Jang, K.; Robins, K. A.; Tran, I. C.; Heske, C.; Lee, D.-C. *Phys. Chem. Chem. Phys.* **2013**, *15*, 5967.
(14) Chung, J. W.; An, B.-K.; Kim, J. W.; Kim, J.-J.; Park, S. Y. *Chem. Commun.* **2008**, 2998−3000.
(15) Mizuno, H.; Ohnishi, I.; Yanagi, H.; Sasaki, F.; Hotta, S. *Adv. Mater.* **2012**, *24*, 2404−2408.
(16) Kiyomura, T.; Nemoto, T.; Yoshida, K.; Minari, T.; Kurata, H.; Isoda, S. *Thin Solid films* **2006**, *515*, 810−813.
(17) Breuer, T.; Witte, G. *Phys. Rev. B* **2011**, *83*, No. 155428.
(18) Reinhardt, J. P.; Hinderhofer, A.; Broch, K.; Heinemeyer, U.; Kowarik, S.; Vorobiev, A.; Gerlach, A.; Schreiber, F. *Phys. Chem. C* **2012**, *116*, 10917−10923.
(19) Brewer, J.; Schiek, M.; Ltzen, A.; Al-Shamery, K.; Rubahn, H.-G. *Nano Lett.* **2006**, *6*, 2656.
(20) Bordo, K.; Schiek, M.; Ghazal, A.; Wallmann, I.; Lützen, A.; Balzer, F.; Rubahn, H.-G. *Phys. Chem. C* **2011**, *115*, 20882−20887.
(21) Novac, J.; Oehzelt, M.; Berkebile, S.; Koini, M.; Ules, T.; Koller, G.; Haber, T.; Resel, R.; Ramsey, M. G. *Phys. Chem. Chem. Phys.* **2011**, *13*, 14675−14684.
(22) Fleming, A. J.; Netzer, F. P.; Ramsey, M. G. *J. Phys.: Condens. Matter* **2009**, *21*, No. 445003.
(23) Fleming, A. J.; Berkebile, S.; Ules, T.; Ramsey, M. G. *Phys. Chem. Chem. Phys.* **2011**, *13*, 4693−4708.
(24) Koller, G.; Berkebile, S.; Krenn, J. R.; Tzvetkov, G.; Hlawacek, G.; Lengyel, O.; Netzer, F. P.; Teichert, C.; Resel, R.; Ramsey, M. G. *Adv. Mater.* **2004**, *16*, 2159.
(25) Resel, R.; Haber, T.; Lengyel, O.; Sitter, H.; Balzer, F.; Rubahn, H.-G. *Surf. Interface Anal.* **2009**, *41*, 764.
(26) Simbrunner, C.; Nabok, D.; Hernandez-Sosa, G.; Oehzelt, M.; Djuric, T.; Resel, R.; Romaner, L.; Puschnig, P.; Ambrosch-Draxl, C.; Salzmann, I.; Schwabegger, G.; Watzinger, I.; Sitter, H. *J. Am. Chem. Soc.* **2011**, *133*, 3056−3062.
(27) Balzer, F.; Rubahn, H.-G. *Surf. Sci.* **2004**, *548*, 170.
(28) Hird, M.; Gray, G. W.; Toyne, K. J. *Mol. Cryst. Liq. Cryst.* **1991**, *206*, 186.
(29) Dingemans, T. J.; Murthy, N. S.; Samulski, E. T. *J. Phys. Chem. B* **2001**, *105*, 8845.
(30) Doetz, F.; Nord, S.; Weiss, H.; Rosch, J. Synthesis of Polynaphthalenes and Their Use. Patent US20070287821 A1, 2007.
(31) Sitter, H.; Andreev, A.; Matt, G.; Sariciftci, N. S. *Mol. Cryst. Liq. Cryst.* **2002**, *385*, 51−60.
(32) Schultz, L. G. *J. Appl. Phys.* **1949**, *20*, 1030.
(33) Pichler, A.; Resel, R.; Neuhold, A.; Zojer, E.; Dingemans, T.; Schwabegger, G.; Simbrunner, C.; Salzmann, I. Unpublished data.
(34) Rappi, A. K.; Casewit, C. J.; Colwell, K. S.; Goddard, W. A., III; Skid, W. M. *J. Am. Chem. Soc.* **1992**, *114*, 10024−10039.
(35) Haber, T.; Andreev, A.; T, A.; Sitter, H.; Oehzelt, M.; Resel, R. *J. Cryst. Growth* **2005**, *284*, 209−220.
(36) Kankate, L.; Balzer, F.; Niehus, H.; Rubahn, H.-G. *Thin Solid Films* **2009**, *518*, 130−137.
(37) Schwabegger, G.; Djuric, T.; Sitter, H.; Resel, R.; Simbrunner, C. *Cryst. Growth Des.* **2013**, *13*, 536−542.
(38) Potocar, T.; Lorbek, S.; Nabok, D.; Shen, Q.; Tumbek, L.; Hlawacek, G.; Puschnig, P.; Ambrosch-Draxl, C.; Teichert, C.; Winkler, A. *Phys. Rev. B* **2011**, *83*, No. 075423.
(39) Hlawacek, G.; Puschnig, P.; Frank, P.; Winkler, A.; Ambrosch-Draxl, C.; Teichert, C. *Science* **2008**, *321*, 108.
(40) Simbrunner, C.; Quochi, F.; Hernandez-Sosa, G.; Oehzelt, M.; Resel, R.; Hesser, G.; Arndt, M.; Saba, M.; Mura, A.; Bongiovanni, G.; Sitter, H. *ACS Nano* **2010**, *4*, 6244−6250.
(41) Bonafede, S. J.; Ward, M. D. *J. Am. Chem. Soc.* **1995**, *117*, 7853−7861.
(42) Carter, P. W.; Ward, M. D. J. *J. Am. Chem. Soc.* **1993**, *115*, 11521−11535.
(43) Simbrunner, C. *Semicond. Sci. Technol.* **2013**, *28*, No. 053001.
(44) Barlow, S.; Raval, R. *Surf. Sci. Rep.* **2003**, *50*, 201−341.
(45) Duncker, K.; Kiel, M.; Höfer, A.; Widdra, W. *Phys. Rev. B* **2008**, *77*, No. 155423.
(46) Valle, R. G. D.; Venuti, E.; Brillante, A.; Girlando, A. *J. Phys. Chem. A* **2008**, *112*, 1085.